AGU PUBLICATIONS

Geophysical Research Letters

RESEARCH LETTER
10.1002/2017GL072668

Key Points:
- We perform experiments to investigate the role of the lithosphere on dynamic topography
- We study the topographic signal of a rising mantle anomaly on the lithosphere
- Surface uplift and bulge aspect ratio are inversely correlated to lithosphere thickness

Correspondence to:
A. Sembroni,
andrea.sembroni@uniroma3.it

Citation:
Sembroni, A., A. Kiraly, C. Faccenna, F. Funiciello, T. W. Becker, J. Globig, and M. Fernandez (2017), Impact of the lithosphere on dynamic topography: Insights from analogue modeling, *Geophys. Res. Lett.*, *44*, 2693–2702, doi:10.1002/2017GL072668.

Received 21 JUN 2016
Accepted 7 MAR 2017
Accepted article online 15 MAR 2017
Published online 23 MAR 2017

Impact of the lithosphere on dynamic topography: Insights from analogue modeling

Andrea Sembroni[1], Agnes Kiraly[1], Claudio Faccenna[1], Francesca Funiciello[1], Thorsten W. Becker[2], Jan Globig[3], and Manuel Fernandez[3]

[1]Department of Science, Roma Tre University, Rome, Italy, [2]Institute for Geophysics, Jackson School of Geosciences, University Texas at Austin, Austin, Texas, USA, [3]Institute of Earth Sciences Jaume Almera (ICTJA-CSIC), Barcelona, Spain

Abstract Density anomalies beneath the lithosphere are expected to generate dynamic topography at the Earth's surface due to the induced mantle flow stresses which scale linearly with density anomalies, while the viscosity of the upper mantle is expected to control uplift rates. However, limited attention has been given to the role of the lithosphere. Here we present results from analogue modeling of the interactions between a density anomaly rising in the mantle and the lithosphere in a Newtonian system. We find that, for instabilities with wavelengths of the same order of magnitude as lithosphere thickness, the uplift rate and the geometry of the surface bulge are inversely correlated to the lithosphere thickness. We also show that a layered lithosphere may modulate the topographic signal. With respect to previous approaches our models represent a novel attempt to unravel the way normal stresses generated by mantle flow are transmitted through a rheologically stratified lithosphere and the resulting topographic signal.

1. Introduction

The topography of our planet is shaped by processes operating at surface, crustal, and lithospheric scales, and at a deeper, mantle level. The latter contribution is usually called "dynamic" when it is due to the viscous stresses driven by convection. The amplitude, wavelength, and rate of surface motion induced by mantle convection are difficult to constrain (for reviews, see *Hager et al.* [1985], *Braun* [2010], and *Flament et al.* [2013]) as they are often masked by the isostatic contribution to topography, considered to be dominant. Regions of mantle upwelling/downwelling can be taken as test sites to constrain the contributions of dynamic topography and how they depend on parameters such as mantle viscosity and lithosphere strength [e.g., *Olson and Nam*, 1986; *Ribe and Christensen*, 1994; *Ribe et al.*, 1995; *Hales et al.*, 2005; *Gogus and Pysklywec*, 2008; *West et al.*, 2009].

Previous analogue models on rising plumes have shown that lithospheric thickness can strongly influence the temporal evolution and maximum amplitude of surface uplift [*Griffiths et al.*, 1989]. More recent numerical models show that rheological stratification of the lithosphere can affect the amplitude and wavelength of topography in a way that may cause complex patterns at smaller scales than those usually assumed in relation to a mantle upwelling [*Burov and Guillou-Frottier*, 2005; *Burov and Gerya*, 2014]. Particularly mechanical decoupling, e.g., a weak lower crust, complicates observation of dynamic topography at the surface due to the interference of crustal and mantle deformation [*Burov and Guillou-Frottier*, 2005]. Despite these results, little work has been done in terms of investigating the influence of different lithosphere configurations (e.g., thickness and viscosity profile of the system) on dynamic topography. Here we perform a set of analogue models to investigate the role of variations in thickness and rheology of the lithosphere on the topography signal generated by a rising, spherical, buoyant mantle instability.

2. Experimental Setup

We study a laboratory analogue of a two layers, viscous lithosphere-upper mantle system using silicone putty-glucose syrup in a tank sized 40 cm × 40 cm × 50 cm (Figure 1). Glucose syrup (mantle) is a Newtonian, low viscosity, high-density fluid, whose transparency allows optical tracing of the rising anomaly. Silicone putty (lithosphere), made of polydimethylsiloxane and iron fillers, is a viscoelastic material that behaves in a quasi-Newtonian fashion if the strain rates during the experiments are low enough to neglect its elastic component, as is the case here [e.g., *Weijermars and Schmeling*, 1986; *Funiciello et al.*, 2003]. The

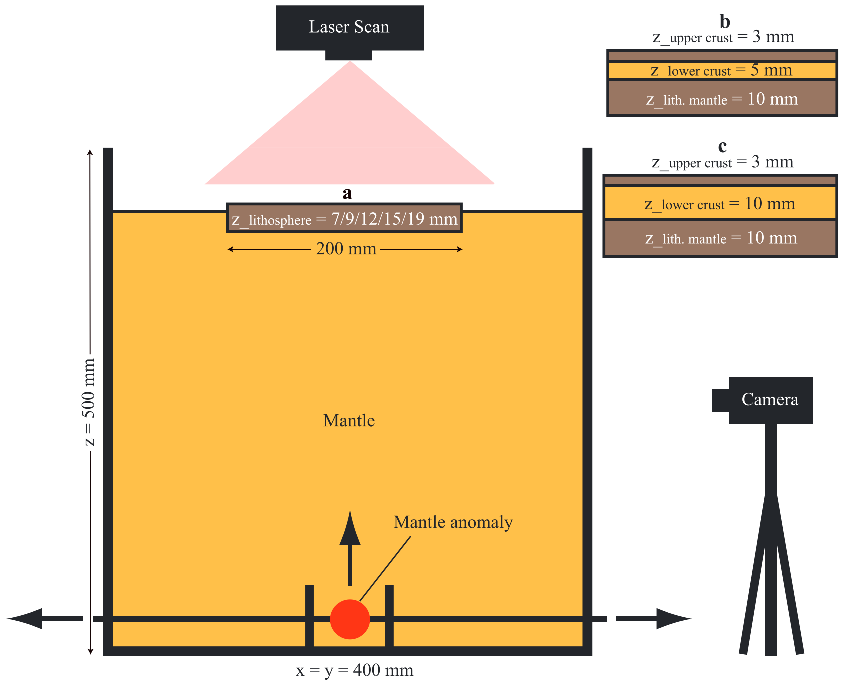

Figure 1. Two-dimensional view of the experimental setup. (a) Homogeneous lithosphere configuration, (b) stratified lithosphere configuration with a 5 mm thick lower crust, and (c) stratified lithosphere configuration with a 10 mm thick lower crust.

mantle upwelling (plume head) is produced by a high viscosity, low-density silicone sphere with a constant radius (15 mm) rising through the mantle. We use a plume radius comparable to the lithosphere thickness to mimic a shallow, lithosphere-scale instability. Unlike natural plumes, the silicone sphere is characterized by a higher viscosity than the surrounding mantle and preserves its shape and volume throughout the model's evolution to facilitate analysis. The experimental system is kept at constant room temperature in order to avoid changes in physical material properties.

Thermal effects and phase changes are neglected, and the dynamics of the whole system is controlled by the interplay between compositional buoyancy and viscous forces. The density difference, ranging from 282 to 308 kg/m^3, between syrup (reference density between 1420 and 1446 kg/m^3) and silicon sphere (density of 1138 kg/m^3), leads to an average rise velocity of ≈2.6 mm/s. This value is slightly lower than the theoretical Stokes velocity (2.8 mm/s) obtained by considering a mantle viscosity of 50 Pa s (see Table 1 and equation (2)). This small discrepancy may be due to surface tension and possible minor boundary effects.

For our experiments, we first place the silicon sphere into the tank, centered and fixed at its bottom by a mechanism composed of two sliding brass skewers. After positioning the 20 × 20 cm^2 "lithospheric plate" on top and attaching it at the center of the tank to prevent plate drifting, the system is left to reach an isostatic, steady state conditions. At the start of the model run, the sphere is released and starts to rise. A side-view camera images the ascending path of the sphere, allowing us to track the sphere location and compute its velocity. A top-view, 3-D scanner (EScan 3-D imaging system) records the evolution of topography from which we can infer the lithospheric uplift rate. To define the wavelength of topography, we use the standard deviation of a best fitting Gaussian curve [see *Kiraly et al.*, 2015].

To test the coupling between the lithosphere and the underlying mantle, we prepare two lithospheric configurations (Figure 1). The first configuration consists of a uniform plate with a variable thickness between 7 and 19 mm (see Table 1). The second, stratified lithosphere configuration is made by embedding a low viscosity layer, which acts as the decoupling "lower crust," in between two identically high viscosity layers representing the upper crust and lithospheric mantle, respectively. For both configurations we test two different lithosphere densities: continental (1300 kg/m^3) and oceanic (1488 kg/m^3). Details about the model setup are provided in Tables 1 and 2.

10.1002/2017GL072668

Table 1. Physical and Scaling Parameters of Laboratory Experiments

		Configuration		Materials	Density (kg/m^3)	Viscosity (Pa x s)	Thickness (mm)
Reference model	Lithosphere	Homogeneous lithosphere	Lithosphere	Silicon (continental) Silicon (oceanic)	1,300 1,488	30,000-32,000 45,000-46,000	7, 9, 12, 15, 19 7, 9, 12, 15, 19
		Stratified lithosphere	Upper crust	Silicon (continental) Silicon (oceanic)	1,300 1,488	30,000-32,000 45,000-46,000	3 3
			Lower crust (decoupling layer)	Low viscous syrup High viscous syrup Silicon	1,420 1,446 940	37-50 178-195 27,000	5, 10 5, 10 5, 10
			Lithospheric mantle	Silicon (continental) Silicon (oceanic)	1,300 1,488	30,000-32,000 45,000-46,000	10 10
	Mantle	-		Low viscous syrup	1,420	37-50	270
	Plume	-		Silicon	1,138	58,000-70,000	15 (radius)
Nature	Lithosphere	Oceanic Continental		- -	3,300 2,900	10^{22}-10^{23} 10^{19}-10^{24}	5-10 x 10^7 4-20 x 10^7
	Mantle	-		-	3,500	10^{20}-10^{22}	2.7 x 10^9
L_{model}/L_{nature}	10^{-7}						
t_{model}/t_{nature}	10^{-13}						

Table 2. Results of the Selected Models[a]

		Experiments	η_m (Pa s)	ρ_m (g/cm^3) (22°C)	η_l (Pa s)	ρ_l (g/cm^3)	η_{DL} (Pa s)	ρ_{DL} (g/cm^3)	W_{max} (mm)	h_{max} (mm)	$v_{s\ max}$ (mm/s)	$h_{d\ max}$ (mm)
Homogeneous lithosphere		CC 7	47.667	1.420	30573.471	1300	-	-	47.872	5.414	0.075	3.275
		CC 9	45.667	1.420	30573.471	1300	-	-	48.008	4.560	0.061	2.372
		CC 12	41.926	1.420	31016.836	1.300	-	-	48.362	3.575	0.043	1.375
		CC 15	41.926	1.420	31016.836	1.300	-	-	47.883	2.988	0.027	1.206
		CC 19	44.383	1.420	30905.169	1.300	-	-	62.714	2.615	0.029	1.597
		OC 7	43.135	1.420	44865.408	1.488	-	-	52.667	5.172	0.062	2.911
		OC 9	44.382	1.420	44960.053	1488	-	-	54.876	4.526	0.049	2.294
		OC 12	42.526	1.420	46491.692	1.488	-	-	55.538	3.774	0.070	1.339
		OC 15	43.136	1.420	46545.953	1.488	-	-	83.763	3.049	0.067	1.830
		OC 19	43.755	1.420	46515.496	1.488	-	-	89.265	2.311	0.040	1.557
Stratified lithosphere	High viscous decoupling layer	CC 10-5-3	44.383	1.420	29975.717	1.200	27.414	0.940	42.142	2.517	0.032	1.304
		CC 10-10-3	43.755	1.420	29398.219	1.143	27.367	0.940	99.311	1.825	0.019	0.910
		OC 10-5-3	43.755	1.420	40383.554	1.336	27.367	0.940	92.853	2.325	0.023	1.056
		OC 10-10-3	43.136	1.420	37533.214	1.250	27.319	0.940	68.454	1.767	0.021	0.736
	Intermediate viscous decoupling layer	CC 10-5-3	41.926	1.420	71910.979	1.341	178.090	1.447	42.142	2.704	0.044	1.882
		CC 10-10-3	42.526	1.420	78600.545	1.364	180.781	1.447	99.311	1.733	0.033	1.200
		OC 10-5-3	45.020	1.420	86039.628	1.476	191.979	1.447	92.853	2.276	0.037	1.479
		OC 10-10-3	45.667	1.420	110335.477	1.470	194.890	1.447	68.454	1.603	0.027	1.024
	Low Viscous decoupling layer	CC 10-5-3	48.354	1.420	35472.933	1.333	48.354	1.420	56.494	1.871	0.025	0.861
		CC 10-10-3	49.759	1.420	38915.085	1.352	49.759	1.420	67.498	1.258	0.013	0.618
		OC 10-5-3	39.054	1.420	43222.958	1.335	39.054	1.420	50.993	2.537	0.032	1.317
		OC 10-10-3	42.526	1.420	43931.627	1.355	42.526	1.420	57.212	2.260	0.032	0.737

[a]The labels OC and CC indicate oceanic and continental crust, respectively. The expressions 10-10-3 and 10-5-3 define the thicknesses (mm) of lithospheric mantle, lower crust, and upper crust used in the experiments. Here η_m is mantle viscosity, ρ_m is the mantle density, η_l is the lithosphere viscosity, ρ_l is the lithosphere density, η_{DL} is the decoupling layer viscosity, ρ_{DL} is the decoupling layer density, W_{max} is the maximum bulge width, h_{max} is the maximum topography, $v_{s\ max}$ is the maximum uplift rate, and $h_{d\ max}$ is the maximum dynamic topography.

A buoyant sphere rising up into a Newtonian viscous mantle exerts a dynamic pressure, P_d, at the surface [e.g., *Morgan*, 1965; *Olson and Nam*, 1986] that is given by

$$P_d = 3\eta_m UR \frac{z}{\left(z^2 + l^2\right)^{3/2}}, \tag{1}$$

where

$$U = \frac{2\Delta\rho_m^s g R^2}{9\eta_m}. \tag{2}$$

$U = \frac{dz}{dt}$ is the Stokes velocity for a solid sphere and t is the time, R is the radius of the sphere, $\Delta\rho_m^s$ is the density difference between sphere and mantle, g is the gravitational acceleration, η_m is the mantle viscosity, z is the depth of—and l is the distance to—the center of the sphere, respectively. The equivalent dynamic topography of amplitude h_d that is induced can be inferred from the total vertical normal stress, σ_{zz}, at the surface by noting that $\sigma_{zz} \approx \Delta\rho_a^l gh$ for long wavelength, small amplitude deflections. Here $\Delta\rho_a^l$ is the density difference at the interface, i.e., between lithosphere and air. On top of the sphere, where $l = z$, this yields after consideration of both pressure and velocity effects for σ_{zz} in the $\frac{z}{R} \gg 1$ limit [*Morgan*, 1965, equation (13)]

$$h_d \approx \frac{2}{3}\frac{1}{2^{3/2}}\frac{\Delta\rho_m^s}{\Delta\rho_a^l}\frac{R^3}{z^2}. \tag{3}$$

Equation (3) shows that dynamic topography, h_d, scales to first order with the buoyancy contrast of the sphere [*Olson and Nam*, 1986], but this equation does not consider the resistance exerted by a shallow, high viscosity layer. Such effects were explored analytically by *Morgan* [1965], for an infinite cylinder, and experimentally by *Griffiths et al.* [1989] and *Kiraly et al.* [2015], showing an inverse relationship with lithospheric thickness.

3. Results

We present results of 22 models (see Table 2), selected from a total of 54 experiments. For each experiment, we consider two distinct phases: dynamic and dynamic-isostatic. The first phase begins when the leading edge of the sphere is at ~80 mm ($5.33 \cdot R$) from the base of the lithosphere. At this depth we start registering an increase in the bulge topography (i.e., dynamic) in agreement with *Griffith et al.* [1989] and *Kiraly et al.* [2015]. As the sphere approaches the base of the plate, the uplift rate reaches its maximum. Once the impact occurs, the new phase begins. Due to its buoyancy, the sphere continues to rise and impinges into the plate. The surface topography reaches a maximum and then it keeps in isostatic equilibrium for the rest of the model.

In the case of the homogeneous lithosphere, the geometry of the topographic signature varies with the thickness and the rheological properties of the plate. In the dynamic phase, by using a 7 mm thick oceanic plate, we obtain a maximum bulge width of ~48 mm, a maximum dynamic topography of ~2.9 mm, and a maximum dynamic uplift rate of 0.062 mm/s (Table 2 and Figure 2). Increasing the thickness of the plate from 7 mm to 19 mm results in up to ~87% laterally wider and lower topography (Table 2 and Figure 2). The strength of the lithosphere also influences the shape of the surface bulge. For a constant thickness, the stronger, denser oceanic lithosphere bulge is larger by ~33% with respect to the continental one, while the maximum dynamic topography shows similar values within ~12% as expected from equation (3) (Figure 2) The maximum values of uplift rate decrease (by up to ~33%) as the thickness of the plate increases in agreement with previous experimental tests [*Griffiths et al.*, 1989; *Kiraly et al.*, 2015]. Moreover, the uplift rate of the weak and lighter continental plate is higher by up to ~10% with respect to the stronger oceanic configuration (Figure 2).

The bulge width and uplift rate decrease dramatically in the dynamic-isostatic phase. On the contrary, the topography keeps increasing after the sphere's arrival at the base of the lithosphere. Between 42 and 56 nondimensionalized time (model time multiplied by Stokes' velocity over the radius of the sphere) the trends of all the curves indicate static equilibrium (Figure 2). The final maximum topography decreases by ~40% when the thickness of the lithosphere increases from 7 to 19 mm (Table 2 and Figure 2).

The stratified lithosphere models show a more complex behavior, which depends not only on the geometry and rheological properties of the plates but also on the nature of the decoupling layer (i.e., lower crust)

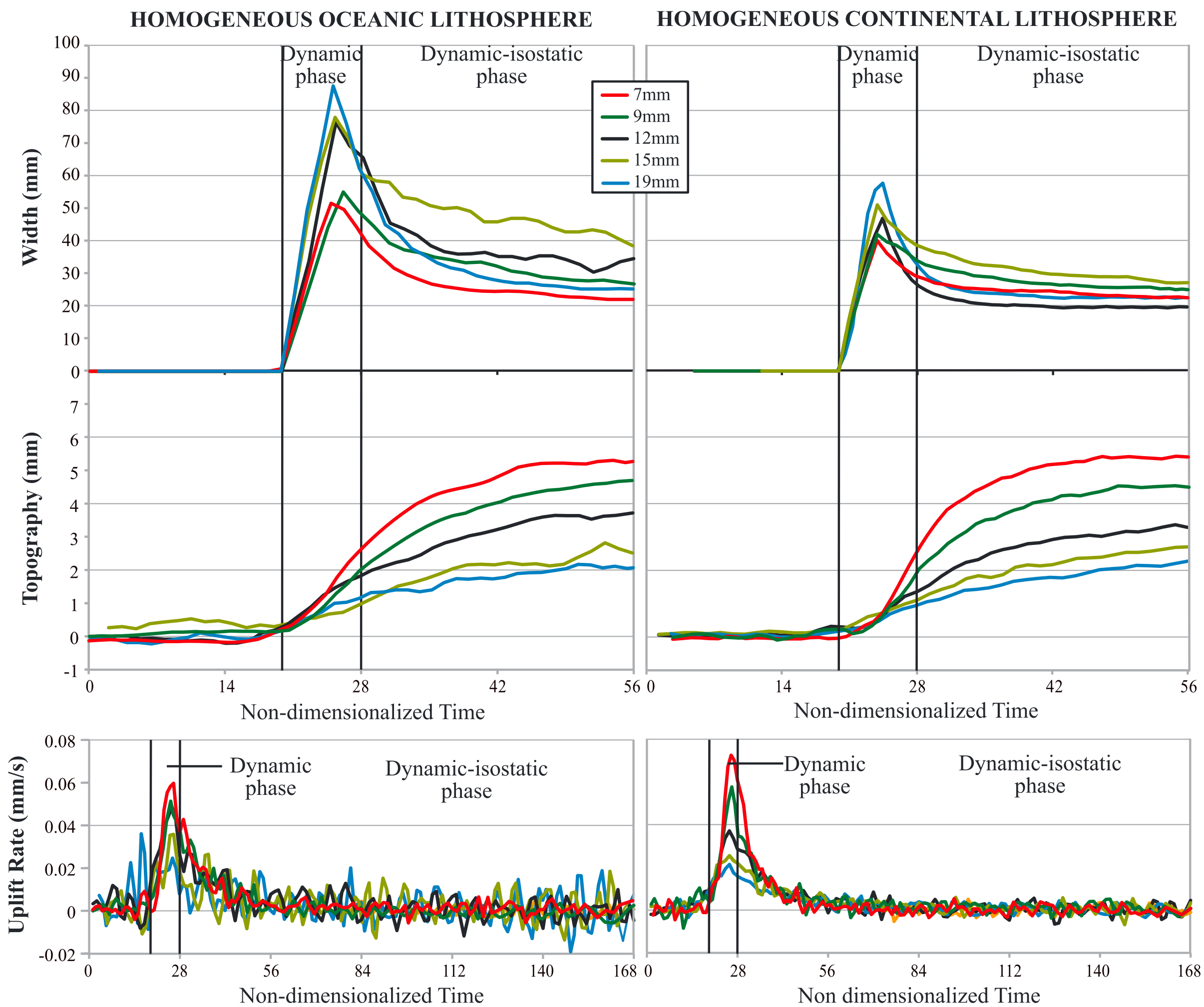

Figure 2. Width, topography, and uplift rate profiles of the homogeneous lithosphere (oceanic and continental) setup models. The curves have been determined using a two-period smoothed moving average algorithm. The width is calculated as a midheight Gaussian width. The sharp maximum in the uplift rate plots is registered when the sphere is 1–6 mm far from the base of the plate. The periodic fluctuations in the uplift rate plots are due to the possible background lightening noise of each experiment. The vertical black line at normalized time 28 indicates the moment when the sphere hits the base of the plate. The time has been non-dimensionalized by dividing it with the ratio between the radius of the sphere and the Stokes' velocity.

(Figure 3). Comparing models with different lithospheric configurations but comparable total lithospheric thickness (i.e., 19 mm homogeneous lithosphere configuration, Figure 1a, and 10/5/3 mm stratified lithosphere configuration, Figure 1b), similar values have been obtained for the maximum topography (Table 2 and Figures 2 and 3). However, an overall decrease in both bulge width and uplift rate is emerging, passing from homogeneous to stratified configurations. The bulge width decreases more significantly (up to 50%) in the presence of a very low viscous decoupling layer (Table 2 and Figures 2 and 3). Moreover, in the case of stratified lithosphere, the uplift rate curves present a strong decrease around 28 nondimensionalized time followed by a second peak (Figure 3). Both features are clearly identified with a low viscous decoupling layer, becoming less clear with a highly viscous layer, and disappearing with a homogeneous lithosphere (Figures 2 and 3).

Doubling the thickness of the decoupling layer (i.e., from 5 to 10 mm) makes the bulge topography lower and narrower of up to 25%. Moreover, a decrease in the uplift rate of up to 35% is recorded. This general decrease is more accentuated for the case of the continental lithosphere (Table 2 and Figure 3).

Figures 4a and 4b show the dependency of the dynamic topography, h_d, and the uplift rate, v_s, (normalized by the quantities of equations (3) and (2), respectively) with the lithosphere thickness and sphere radius (L/R). The wavelength of the instabilities is of the same order of magnitude as the lithosphere thickness,

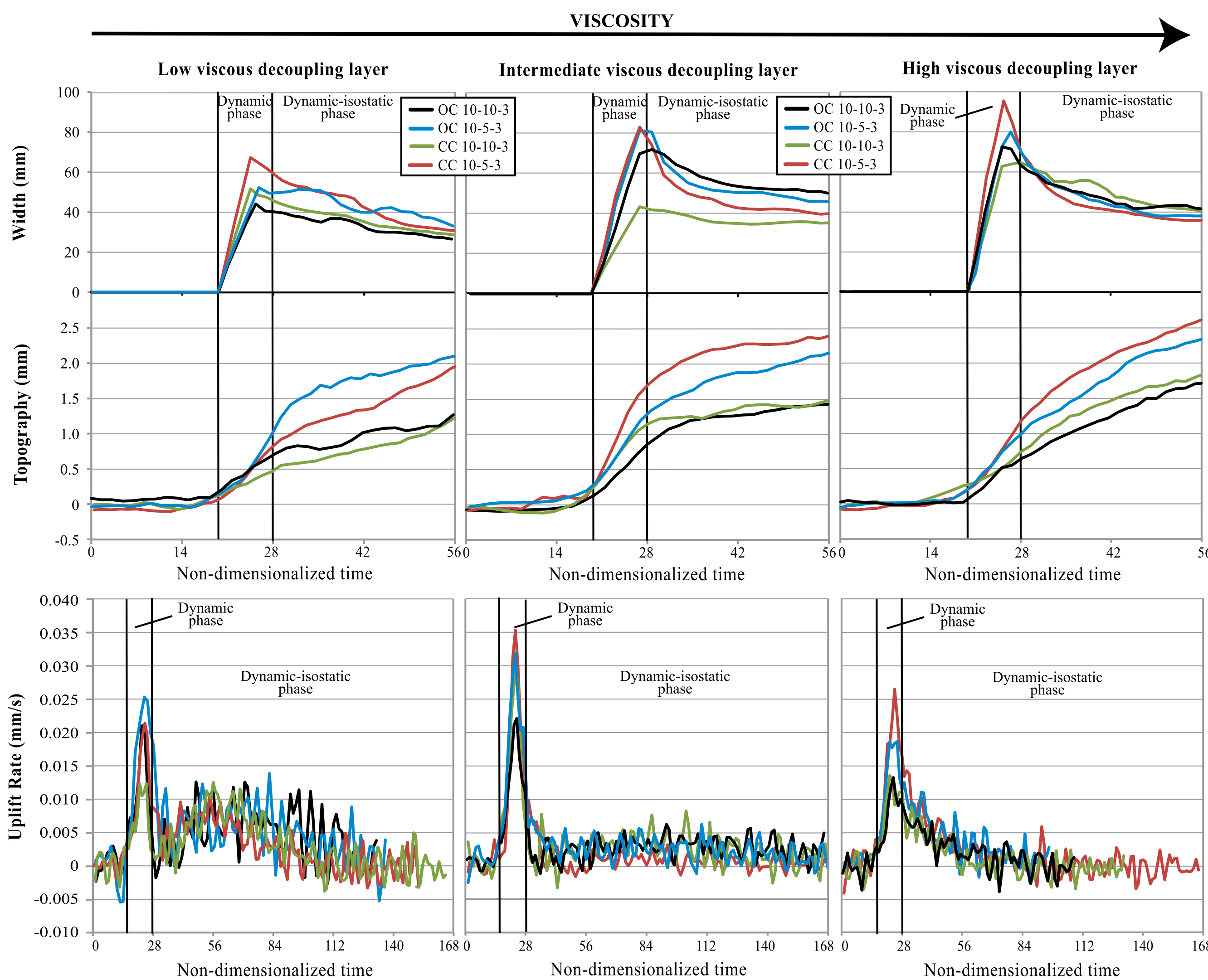

Figure 3. Width, topography and uplift rate profiles of the stratified lithosphere (oceanic and continental) setup models. The curves have been determined using a two-period smoothed moving average algorithm. The labels OC and CC indicate oceanic and continental crust, respectively. The expressions 10-10-3 and 10-5-3 define the thicknesses (mm) of lithospheric mantle, lower crust, and upper crust, respectively.

meaning that some of the theoretical assumptions are violated. Yet the scalings still remain useful as is shown by nondimensionalized properties being of order unity.

Figure 4c shows how the bulge width depends upon the lithosphere thickness. In particular the results obtained with the stratified lithosphere configuration deviate from the homogeneous lithosphere trend (Figure 4c). Such deviation is likely caused by the difference in strength between homogeneous and stratified lithosphere configurations. The departure from the prediction is evident in the low strength layered lithosphere ("continental") that shows a lower flexural strength with respect to the higher strength "oceanic" one (Figure 4c).

4. Discussion and Final Remarks

The experimental results illustrate a clear dynamic topography signal with the uplift rate reaching its maximum just before the sphere hits the base of the lithosphere. After that, the uplift rate decreases and topography reaches an isostatic equilibrium configuration, as was found by *Griffiths et al*. [1989]. The aim of our experiments was to explore the role played by the lithosphere. Our study shows that the uplift rate and the geometry of the surface bulge (i.e., width and elevation) are strongly influenced by the mechanical

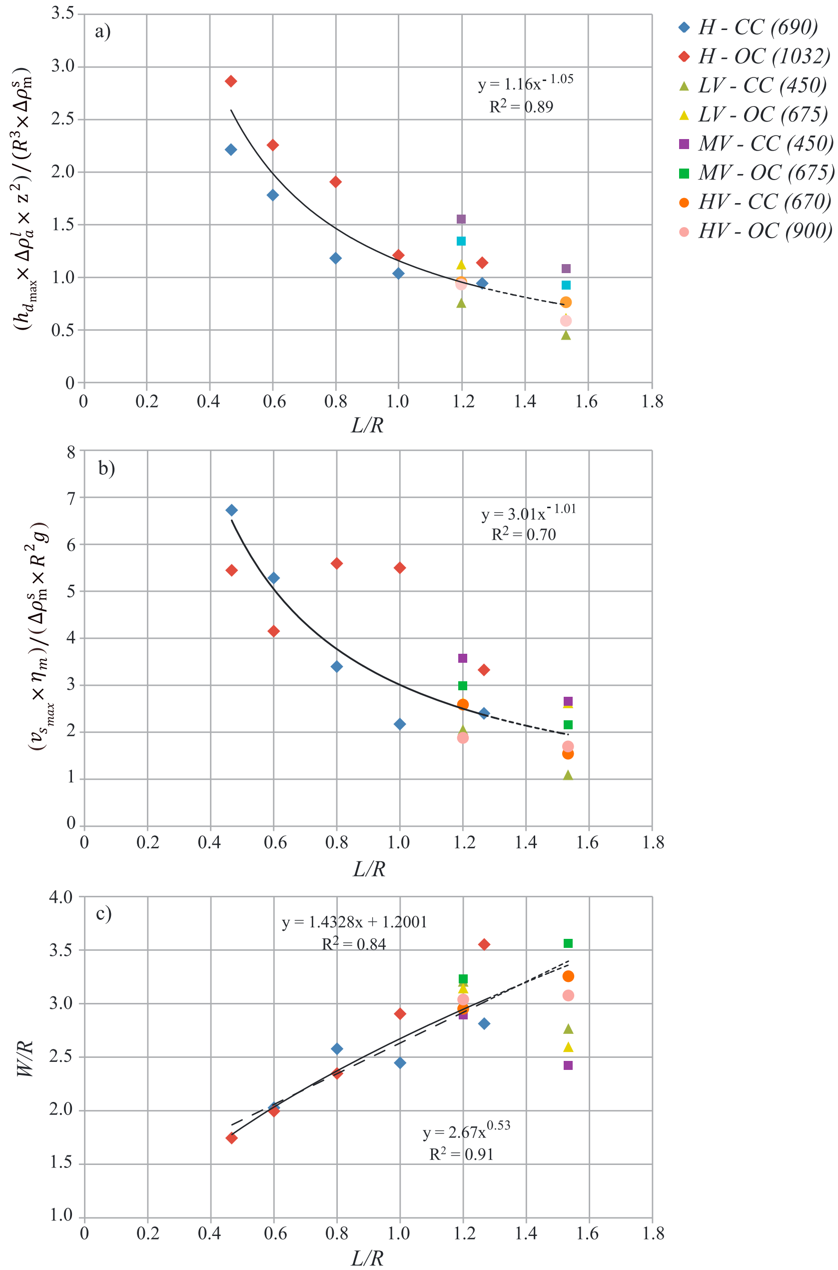

Figure 4. Results from 22 experiments: (a) Dynamic topography, h_d, normalized by the Stokes sphere estimate, equation (3), versus lithospheric thickness, *L*, normalized by plume radius, *R*. (b) Uplift rate, *v*, normalized by the Stokes velocity, equation (2), versus *L*/*R*. (c) Normalized width of the bulge, *W*/*R*, versus normalized thickness, *L*/*R*. Values in the legend indicate the coupling between lithosphere and mantle. Data have been fit by power laws.

properties of the lithosphere (Figure 4). This is in agreement with previous experimental studies [*Griffiths et al.*, 1989; *Kiraly et al.*, 2015], but our results are able to highlight this difference over a larger range of lithosphere/mantle coupling. Moreover, our results show that the uplift rate and the dynamic topography of the surface bulge are inversely related to the lithosphere thickness (Figures 4a and 4b). Both $h_{d_{\max}}$ and $v_{s_{\max}}$ decrease as ~ $(L/R)^{-1}$, in contrast to the estimates of *Griffiths et al.* [1989], which suggest a decrease of $(L/R)^{-2}$ for lithosphere thicker than 4 mm, and higher than the value of *Olson and Nam* [1986; $(L/R)^{-1/2}$]. Moreover, the influence of the lithosphere becomes asymptotic at ~0.4 *L*/*R* (Figures 4a and 4b). We also show that increasing the lithosphere/mantle coupling of up to 3 orders of magnitude increases the dependency of the surface signal (uplift rate and amplitude) upon the thickness of the lithosphere.

Investigation over a wider range of parameters and additional numerical experiments and theoretical analysis are needed to obtain more robust information on the scaling laws between lithosphere rheology and dynamic topography signal.

The presence of a decoupling lower crust leads to a decrease in bulge width and uplift rate with respect to the homogeneous case (Figure 3). In particular, the thicker and less viscous the lower crust, the lower and narrower the topography signal (Figure 3). The presence of a decoupling layer also strongly influences the amplitude of the uplift rate (Figure 3). In the case of the stratified lithosphere, the uplift rate plots are characterized by two peaks, the second of which occurs long after the arrival of the anomaly at the base of the lithosphere. Such signal increases with the decrease of the viscosity of the decoupling layer (Figure 3), and, as expected, it flattens out for a higher decoupling layer viscosity (see Figures 2 and 3). Numerical models [e.g., *Burov and Guillou-Frottier*, 2005; *Burov and Gerya*, 2014] highlight that thick, rheologically stratified lithosphere filters the mantle flow patterns generating complex uplift patterns. We interpret this second uplift signal as related to unloading due to the outward lower crust flow from the impact point of the ascending sphere. Once the mantle anomaly hits the base of the lithosphere it produces an outward, downhill flow of the decoupling layer, thinning and unloading the lithosphere layer itself. The lithosphere thinning can explain the second peak of uplift. Hence, while the first peak of uplift is purely dynamic, the second one is the result of the combination of dynamic forces and isostatic processes. The viscosity of the lower crust also influences the amplitude of topography. By increasing the viscosity, the deflection becomes lower and wider. This effect may be particularly relevant in natural systems, for example, when a plume impinges under a continental lithosphere such as beneath Afar or Massif Central, where uplift may have lasted for tens of millions years [e.g., *Sembroni et al.*, 2016; *Olivetti et al.*, 2016].

In conclusion, our models illustrate that estimates of dynamic topography should take into account not only the wavelength of the mantle anomaly [cf. *Richards and Hager*, 1984; *Colli et al.*, 2016] but also the rheological properties of the lithosphere, which is often neglected [cf. *Burov and Diament*, 1992], and that the presence of a weak lower crust layer strongly affects the uplift pattern. This dependence may be particularly relevant for the case of shallow instabilities, where wavelengths are usually of the same order of magnitude as lithosphere thickness.

Acknowledgments

The authors thank Taras Gerya and an anonymous reviewer for their helpful comments on an earlier version of this manuscript. T.W.B. was partially supported through NASA OSP 201601412-001. Data associated with this study can be obtained upon request from the author (email: andrea.sembroni@uniroma3.it).

References

Braun, J. (2010), The many surface expressions of mantle dynamics, *Nat. Geosci.*, *3*(12), 825–833, doi:10.1038/ngeo1020.

Burov, E. B., and M. Diament (1992), Flexure of the continental lithosphere with multilayered rheology, *Geophys. J. Int.*, *109*(2), 449–468.

Burov, E., and L. Guillou-Frottier (2005), The plume-head continental lithosphere interaction using a tectonically realistic formulation for the lithosphere, *Geophys. J. Int.*, *58*, doi:10.1111/j.136.-246x.2005.02588.x.

Burov, E., and T. Gerya (2014), Asymmetric three-dimensional topography over mantle plumes, *Nature*, *513*, 85–89, doi:10.1038/nature13703.

Colli, L., S. Ghelichkhan, and H. P. Bunge (2016), On the ratio of dynamic topography and gravity anomalies in a dynamic Earth, *Geophys. Res. Lett.*, *43*, 2510–2516, doi:10.1002/2016GL067929.

Flament, N., M. Gurnis, and R. Dietmar Müller (2013), A review of observations and models of dynamic topography, *Lithosphere*, *5*(2), 189–210, doi:10.1130/L245.1.

Funiciello, F., C. Faccenna, D. Giardini, and K. Regenauer-Lieb (2003), Dynamics of retreating slabs: 2. Insights from three-dimensional laboratory experiments, *J. Geophys. Res.*, *108*(B4), 2207, doi:10.1029/2001JB000896.

Gogus, O., and R. Pysklywec (2008), Near surface diagnostics of dripping and delaminating lithosphere, *J. Geophys. Res.*, *113*, B11404, doi:10.1029/2007JB005123.

Griffiths, R. W., M. Gurnis, and G. Eitelberg (1989), Holographic measurements of surface topography in laboratory models of mantle hotspots, *Geophys. J. Int.*, *96*(3), 477–495, doi:10.1111/j.1365-246X.1989.tb06009.x.

Hager, B. H., R. W. Clayton, M. A. Richards, R. P. Comer, and A. M. Dziewonski (1985), Lower mantle heterogeneity, dynamic topography and the geoid, *Nature*, *313*, 541–545.

Hales, T. C., D. L. Abt, E. D. Humphreys, and J. J. Roering (2005), A lithospheric origin for Columbia River flood basalts and Wallowa Mountains uplift in northeast Oregon, *Nature*, *438*, 842–845, doi:10.1038/nature04313.

Kiraly, A., C. Faccenna, F. Funiciello, and A. Sembroni (2015), Coupling surface and mantle dynamics: A novel experimental approach, *Geophys. Res. Lett.*, *42*, 3863–3869, doi:10.1002/2015GL063867.

Morgan, W. J. (1965), Gravity anomalies and convection currents: 1. A sphere and a cylinder sinking beneath the surface of a viscous fluid, *J. Geophys. Res.*, *70*, 6175–6187, doi:10.1029/JZ070i024p06175.

Olivetti, V., G. Godard, G. Bellier, and ASTER team (2016), Cenozoic rejuvenation events of Massif Central topography (France): Insights from cosmogenic denudation rates and river profiles, *Earth Planet. Sci. Lett.*, *444*, 179–191, doi:10.1016/j.epsl.2016.03.049.

Olson, P., and I. S. Nam (1986), Formation of seafloor swells by mantle plumes, *J. Geophys. Res.*, *91*, 7181–7191, doi:10.1029/JB091iB07p07181.

Ribe, N. M., and U. R. Christensen (1994), The dynamical origin of Hawaiian volcanism, *Earth Planet. Sci. Lett.*, *171*, 517–531.

Ribe, N. M., U. R. Christensen, and J. Theiβing (1995), The dynamics of plume-ridge interaction, 1: Ridge-centered plumes, *Earth Planet. Sci. Lett.*, *134*, 155–168.

Richards, M. A., and B. H. Hager (1984), Geoid anomalies in a dynamic Earth, *J. Geophys. Res.*, *89*, 5987–6002, doi:10.1029/JB089iB07p05987.

Sembroni, A., C. Faccenna, T. W. Becker, P. Molin, and B. Abebe (2016), Longterm, deep-mantle support of the Ethiopia-Yemen Plateau, *Tectonics*, *35*, 469–488, doi:10.1002/2015TC004000.

Weijermars, R., and H. Schmeling (1986), Scaling of Newtonian and non-Newtonian fluid dynamics without inertia for quantitative modelling of rock flow due to gravity (including the concept of rheological similarity), *Phys. Earth Planet. Inter.*, *43*, 316–330.

West, J. D., M. J. Fouch, and J. B. Roth (2009), Vertical mantle flow associated with a lithospheric drip beneath the Great Basin, *Nat. Geosci.*, *2*, 438–443.